Inorganic Chemistry

Article

pubs.acs.org/IC

Influence of the Electronic Configuration in the Properties of d^6–d^5 Mixed-Valence Complexes

German E. Pieslinger, Bruno M. Aramburu-Trošelj, Alejandro Cadranel, and Luis M. Baraldo*

Departamento de Química Analítica, Inorgánica y Química Física, INQUIMAE, Facultad de Ciencias Exactas y Naturales, Universidad de Buenos Aires, Pabellón 2, Ciudad Universitaria, C1428EHA, Buenos Aires, Argentina

Supporting Information

ABSTRACT: We report here the spectroscopic properties of four very closely related mixed-valence cyanide-bridged bimetallic complexes, *trans*-[Ru(T)(bpy)(μ-NC)Ru-(L)$_4$(CN)]$^{3+}$ (T = tris(1-pyrazolyl)methane (tpm, **a**) or 2,2′;6′,2″-terpyridine, (tpy, **b**), and L = pyridine (py, **1**) or 4-methoxypyridine (MeOpy, **2**)). In acetonitrile all the complexes present intervalence charge transfer (IVCT) transitions in the NIR region, but their intensities are widely different, with the intensity of the transition observed for **1a**–**b**$^{3+}$ around four times larger than that observed for **2a**–**b**$^{3+}$. This contrasting behavior can be traced to the different nature of the dπ acceptor orbitals involved in these transitions, as confirmed by (TD)DFT calculations. The spectroscopy of **1a**–**b**$^{3+}$ provides evidence that the spin density is delocalized over the two ruthenium ions, such as a narrowing of the IVCT bands that results in the resolution of the expected three bands, and a weak solvent dependence of the energy of these transitions. The spectroscopy of **2a**–**b**$^{3+}$ instead indicates that the spin density is localized on one ruthenium ion. The IVCT in these systems is particularly weak due to the configuration of the Ru(III), where the vacant orbital is perpendicular to the cyanide bridge.

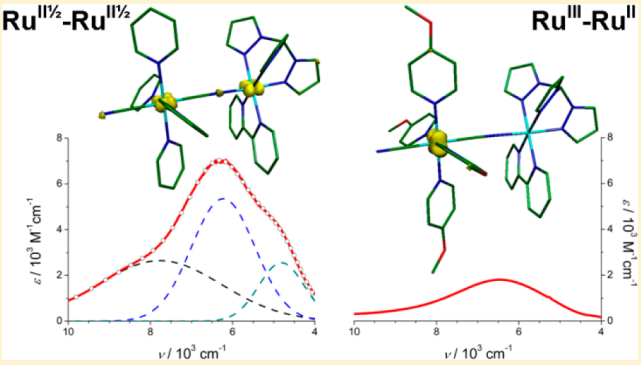

INTRODUCTION

The spectroscopy of mixed-valence complexes has been explored for over four decades since the original report of the properties of the Creutz–Taube ion.[1] Among the explored bridges, the cyanide ion has been frequently explored and it has been shown to be able to promote efficient electronic[2] and magnetic[3] communication between the connected units, both in ground and in electronically excited states. In spite of these properties, until recently[4,5] all the reported systems presented a localized ground state.

In the exploration of mixed valence systems, the d^6–d^5 configuration figures prominently due to the ready availability of the iron, ruthenium, and osmium (II/III) couples. The properties of the observed IVCT transition have usually been treated with a semiclassical theoretical approximation[6−9] where only one orbital interaction is assumed. This approach neglects the influence of the configuration of the ions in the properties of the IVCT transitions. For example, for a d^6–d^5 system, the lack of octahedral symmetry may split the dπ orbitals. In this case, three IVCT transitions are expected[10] together with two transitions between the split dπ orbitals (intraconfigurational, IC), a prediction that has been confirmed experimentally.[11−13] Similarly, different spectroscopies might be observed depending on the orientation of dπ acceptor orbital. If the acceptor orbital lies perpendicular to the bridge, a weaker transition is expected.

Here we show the properties of four closely related cyanide-bridged bimetallic complexes, *trans*-[Ru(T)(bpy)(μ-NC)Ru-(L)$_4$(CN)]$^{2+/3+/4+}$ (T = tris(1-pyrazolyl)methane (tpm, **a**) or 2,2′;6′,2″-terpyridine, (tpy, **b**), and L = pyridine (py, **1**) or 4-methoxypyridine (MeOpy, **2**)), where a ruthenium polypyridine fragment (Ru$_{pp}$) is linked to a substituted dicyanide ruthenium tetrapyridine (Ru$_{py}$) (Figure 1). The mixed-valence complexes reported present an unusual variation on the properties of the IVCT bands, which can be traced to the different nature of the acceptor orbitals on the Ru$^{III}_{py}$ moiety, as suggested by the DFT calculations performed for these systems. This offers a unique opportunity to evaluate the impact of very different metal–metal coupling in otherwise very similar bimetallic complexes.

EXPERIMENTAL SECTION

Materials. The compounds [Ru^{II}(tpm)(bpy)(OH$_2$)](ClO$_4$)$_2$,[14] [Ru^{II}(tpy)(bpy)(OH$_2$)](ClO$_4$)$_2$,[15] *trans*-[Ru^{II}(py)$_4$(CN)$_2$],[16] *trans*-[Ru^{II}(MeOpy)$_4$(CN)$_2$],[17] and *trans*-[(T)(bpy)Ru^{II}(μ-NC)-Ru^{II}(py)$_4$(CN)](PF$_6$)$_2$[18] (T = tpm (**1a**) or tpy (**1b**)) were prepared according to previous reports. Solvents for spectroelectrochemical measurements were dried using a PureSolv Micro solvent purification system. All other reagents were obtained commercially and used as supplied. The new compounds synthesized were dried in a vacuum desiccator for at least 12 h prior to characterization.

Synthesis. *trans-[(T)(bpy)Ru^{II}(μ-NC)Ru^{II}(MeOpy)$_4$(CN)](PF$_6$)$_2$ (T = tpm (**2a**) or tpy (**2b**)).* 0.14 mmol of [Ru^{II}(T)(bpy)(OH$_2$)](ClO$_4$)$_2$

Received: January 31, 2014
Published: July 28, 2014

   dx.doi.org/10.1021/ic5002539 | *Inorg. Chem.* 2014, 53, 8221–8229

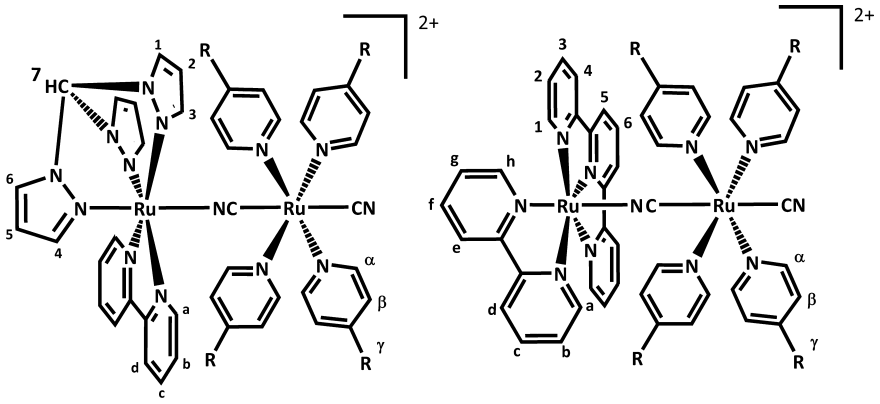

Figure 1. Structures of the complexes **1a** (left, R = H), **2a** (left, R = OCH_3), **1b** (right, R = H), **2b** (right, R = OCH_3). Labels identify hydrogen atoms according to NMR assignments.

(T = tpy, 100 mg, T = tpm, 96.4 mg) and 1.02 mmol of *trans*-$[Ru^{II}(MeOpy)_4(CN)_2]$ (600 mg) were dissolved in 140 mL of water/methanol (1:1) and heated under reflux for 5 h. After the mixture cooled down, the solvents were removed under vacuum, and the resulting solid was suspended in acetonitrile (10 mL). The insoluble excess of *trans*-$[Ru^{II}(MeOpy)_4(CN)_2]$ was removed by filtration, and the dark solution was evaporated to dryness. The remaining solid was dissolved in a minimum volume of methanol and loaded on a Sephadex LH-20 column (l = 30 cm, ⌀ = 4 cm) packed and eluted with methanol. The second of three fractions obtained presented a dark brown (L = tpy) or deep orange (L = tpm) color and was evaporated until dryness. The solid was dissolved in acetone (2 mL), and saturated aqueous NH_4PF_6 was added. After standing overnight at 4 °C, the solid was collected by filtration, washed with chilled water, and dried under vacuum. T = tpm: yield 92 mg (38%). Anal. Calcd for $C_{46}H_{46}N_{14}O_4P_2F_{12}Ru_2{\cdot}H_2O$: C, 40.4; H, 3.53; N, 14.3. Found: C, 40.7; H, 3.50; N, 13.9. ^{1}H NMR (CD_3OD, 500 MHz) δ (ppm): 9.53 (s, 1H, H7), 8.76 (d, 2H, Ha), 8.66 (d, 2H, Hd), 8.53 (d, 2H, H1), 8.41 (d, 1H, H4), 8.23 (d, 2H, H3), 8.18 (dd, 2H, Hc), 7.91 (d, 8H, Hα), 7.64 (dd, 2H, Hb), 6.85 (d, 1H, H6), 6.79 (d, 2H, H2), 6.63 (d, 8H, Hβ), 6.39 (d, 1H, H5), 3.87 (s, 12H, Hγ). T = tpy: yield 87 mg (45%). Anal. Calcd $C_{51}H_{47}N_{11}O_4P_2F_{12}Ru_2$: C, 44.7; H, 3.5; N, 11.2. Found: C, 44.7; H, 3.5; N, 11.1. ^{1}H NMR (CD_3OD, 500 MHz) δ (ppm): 9.92 (ddd, 1H, Ha), 8.92 (d, 1H, Hd), 8.90 (d, 2H, H5), 8.74 (ddd, 2H, H4), 8.65 (d, 1H, He), 8.46 (t, 1H, H6), 8.43 (ddd, 1H, Hc), 8.17 (ddd, 2H, H3), 8.03 (ddd, 2H, H1), 8.02 (ddd, 1H, Hb), 7.98 (dd, 8H, Hα), 7.91 (ddd, 1H, Hf), 7.71 (ddd, 1H, Hh), 7.56 (ddd, 2H, H2), 7.21 (ddd, 1H, Hg), 6.62 (dd, 8H, Hβ), 3.89 (s, 12H, Hγ).

Physical Measurements. NIR and IR spectra were collected in solution with a Nicolet iS10 FT-IR spectrometer (range 12000−400 cm^{-1}). UV−visible spectra were recorded with a Hewlett-Packard 8453 diode array spectrometer (range 190−1100 nm). Optimal Gaussian deconvolution of the experimental spectra were performed using the solver function in a Microsoft Excel spreadsheet. ^{1}H NMR spectra were measured with a Bruker ARX500 spectrometer, using deuterated solvents from Aldrich. Elemental analyses were carried on a Carlo Erba 1108 analyzer. Cyclic voltammetry measurements were performed under argon with millimolar solutions of the compounds, using a TEQ V3 potentiostat and a standard three electrode arrangement consisting of a glassy carbon disc (area = 9.4 mm^2) as the working electrode, a platinum wire as the counter electrode, and a silver wire as reference electrode plus an internal ferrocene (Fc) standard. Tetra-*n*-butylammonium hexafluorophosphate ([TBA]PF_6, 0.1 M) was used as the supporting electrolyte in acetonitrile. All the potentials reported in this work are referenced to the standard Ag/AgCl saturated KCl electrode (0.197 V vs NHE), the conversions being performed with literature values for the Fc^+/Fc couple in different media.[19] All the spectroelectrochemical (SEC) experiments were performed using a three-electrode OTTLE cell,[20] with millimolar solutions of the compounds using [TBA]PF_6 0.1 M as the supporting electrolyte.

Theoretical Methods. Density functional theory (DFT) computations were employed to fully optimize the geometries of the three redox states of *trans*-$[(T)(bpy)Ru(\mu\text{-}NC)Ru(L)_4(CN)]^{n+}$ (n = 2−4) in vacuum and acetonitrile, without symmetry constraints. The calculations were done with the *Gaussian09* package,[21] at the B3LYP level of theory using restricted and unrestricted approximations of the Kohn−Sham equations, depending on the total number of electrons.[22] In all cases, the effective core potential basis set LanL2DZ was employed, which proved to be suitable for geometry predictions in coordination compounds containing metals of the second row of the transition elements in the periodic table. Solvation effects were accounted for using the most recent implementation of the implicit IEF-PCM solvation model.[23−25] Tight SCF convergence criteria and default settings were used in the geometry optimizations. IR calculations and all optimized structures were confirmed as minima by analyzing the harmonic vibrational frequencies.[26] Vertical electronic excitation energies and intensities were evaluated using the time-dependent DFT ((TD)DFT)[27,28] approach with the *Gaussian09* package,[21] and the isodensity plots of the orbitals involved in these transitions were visualized using *Molekel*.[29,30] *GaussSum*[31] software was used to perform spectral simulation and to extract molecular orbital information. The calculated low-energy absorption spectra, the composition of electronic transitions, the associated molecular orbitals, and the Mulliken spin densities for the four mixed-valence complexes are shown in the Supporting Information.

RESULTS

Electrochemistry. Cyclic voltammograms in acetonitrile for all the complexes presented here show two reversible waves at anodic potentials (Figure 2), ascribable to the two ruthenium

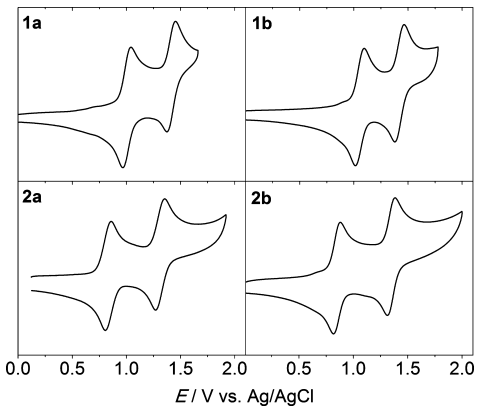

Figure 2. Cyclic voltammograms of **1a**, **1b**, **2a**, and **2b** in acetonitrile/0.1 M [TBA]PF_6 at 100 $mV{\cdot}s^{-1}$ scan rate.

dx.doi.org/10.1021/ic5002539 | *Inorg. Chem.* 2014, 53, 8221−8229

(III/II) couples of the bimetallic compounds (Table 1). For **2a–b** the oxidation at lower potentials is located at the Ru_{py}

Table 1. Reduction Potentials of the Complexes 1a–b and 2a–b in Acetonitrile/0.1 M [TBA]PF_6

			$E_{1/2}$ (ΔE_p)/V (mV)		
complex	T	L	$Ru_{py}^{III/II}$	$Ru_{PP}^{III/II}$	ΔE/V
1a	tpm	py	1.00 (70)	1.41 (80)	0.41
1b	tpy	py	1.05 (90)	1.42 (90)	0.37
2a	tpm	MeOpy	0.83 (100)	1.33 (110)	0.50
2b	tpy	MeOpy	0.85 (65)	1.35 (75)	0.50
$[Ru(py)_4(CN)_2]$			0.85 (70)		
$[Ru(MeOpy)_4(CN)_2]$			0.67 (70)		
$[Ru(tpm)(bpy)(NCS)]^+$				0.96 (100)	
$[Ru(tpy)(bpy)(NCS)]^+$				1.04 (90)	

center, as confirmed by IR and vis–NIR spectroelectrochemistry and supported by DFT calculations (vide infra), even though the redox potential of this fragment is higher in **2a–b** than in the associated monomer (E° = 0.67 V in acetonitrile[17]) due to the coordination of the cationic fragment Ru_{pp}^{2+} to the cyanide. For Ru_{pp}, the polypyridinic ligands have a larger degree of conjugation than pyridines, and consequently a more pronounced acceptor character, stabilizing the ruthenium(II) moieties and shifting their oxidation potentials anodically. This difference between the iminic ligands is large enough to overcome the redox asymmetry imposed by the cyanide bridge, whose orientation can be deduced from the synthetic procedures and is evidenced in the crystal structure of **1b**.[18] The observed ΔE of 0.50 V for **2a–b** is mainly due to the different nature of the coordination spheres of the ruthenium fragments.

For **1a–b**, the assignment of the electronic configuration of the mixed-valence species is less clear. The replacement of MeOpy ligand by pyridine should result in an increase of 0.20 V in the redox potential of the Ru_{py} center,[17] and hence in a decrease of the ΔE between the ruthenium couples of the same amount. However, the ΔE for **1a–b**$^{2+}$ average 0.4 V instead of 0.3 V (Table 1), which indicates an enhanced stability for the mixed-valence complexes **1a–b**$^{3+}$.

UV–Vis–NIR Spectroscopy. All the absorption profiles of the [II,II] species in the near UV–visible (black lines) are governed by π(pp) → π^*(pp) LC signals above 30000 cm^{-1} and two MLCT sets, one stronger corresponding to the d$\pi(Ru_{py})$ → π^*(py) transitions (27000–30000 cm^{-1}) and weaker d$\pi(Ru_{pp})$ → π^*(pp) transitions around 20000 cm^{-1} (Table 2). Upon one electron oxidation (Figure 3 and Figure S2 in the Supporting Information right panels, red line), **2a–b**$^{3+}$ show the typical and intense π(MeOpy) → d$\pi(Ru_{py})$ LMCT transitions at ~21500 cm^{-1},[17] together with the disappearance of the d$\pi(Ru_{py})$ → π^*(py) MLCT transitions, which provides unequivocal evidence of the presence of a Ru_{py}^{III} fragment in these systems. Although the LMCT bands obscure the expected blue shift in the d$\pi(Ru_{pp})$ → π^*(pp) MLCT, shoulders at 28800 and 28200 cm^{-1}, for **2a**$^{3+}$ and **2b**$^{3+}$ respectively, can be assigned as the high energy components

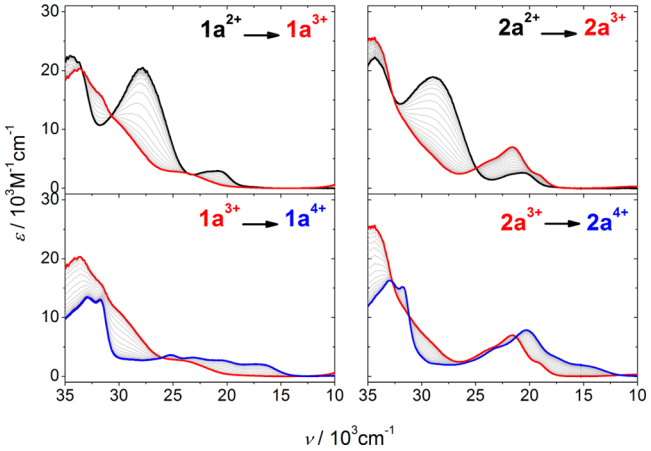

Figure 3. Vis–NIR spectroelectrochemistry of **1a** (left) and **2a** (right) in acetonitrile/0.1 M [TBA]PF_6, during the first (top) and second (bottom) oxidation processes. The spectra of the [II,II] (black), [II,III] (red), and [III,III] (blue) species are highlighted.

Table 2. Vis–NIR Data in Acetonitrile/0.1 M [TBA]PF_6 for the Complexes 1a–b$^{2+/3+}$ and 2a–b$^{2+/3+}$

	$\nu_{max}/10^3$ cm^{-1} ($\varepsilon_{max}/10^3$ M^{-1} cm^{-1}) [$\Delta\nu_{1/2}/10^3$ cm^{-1}]				
complex	LC $\pi \rightarrow \pi^*$	MLCT d$\pi(Ru_{py}) \rightarrow \pi^*$(py)	MLCT d$\pi(Ru_{pp}) \rightarrow \pi^*$(pp)	LMCT π(py) → d$\pi(Ru_{py})$	IVCT
1a^{2+}	34.5 (22.4)	28.0 (20.4)	20.9 (3.0)		
1a^{3+}	33.5 (20.0)	31.6 (15.8)sh	29.1 (8.8)sh		7.8 (2.0) [3.5]^a
			23.2 (2.5)sh		6.2 (5.4) [1.8]^a
					4.8 (2.6) [1.3]^a
1b^{2+}	35.5 (35.5)	27.9 (23.5)	20.9 (7.4)		
	34.3 (38.1)				
	31.8 (37.7)				
1b^{3+}	35.2 (38.9)		30.2 (21.4)sh		7.1 (2.5) [3.5]^a
	32.4 (34.5)		23.2 (5.4)		6.0 (5.1) [2.0]^a
					4.5 (1.8) [2.4]^a
2a^{2+}	34.3 (22.0)	29.0 (18.9)	20.7 (2.6)		
2a^{3+}	34.5 (25.6)	28.8 (5.6)sh		21.6 (7.0)	6.5 (1.8) [2.9]
2b^{2+}	34.3 (35.9)	28.5 (22.3)sh	21.8 (6.7)		
	31.6 (37.3)				
2b^{3+}	34.8 (36.5)		30.5 (16.4)sh	21.5 (13.6)	7.0 (1.0) [3.8]
	32.2 (33.6)				

^{a}Spectral parameters obtained by Gaussian deconvolution with spectral fitting procedures (see Figure S9 in the Supporting Information).

dx.doi.org/10.1021/ic5002539 | Inorg. Chem. 2014, 53, 8221–8229

Table 3. Vis−NIR Data in Acetonitrile/0.1 M [TBA]PF_6 for the Complexes 1a−b^{4+} and 2a−b^{4+}

		$\nu_{max}/10^3$ cm^{-1} ($\varepsilon_{max}/10^3$ M^{-1} cm^{-1})		
complex	LC $\pi \rightarrow \pi^*$	LMCT π(py) → dπ(Ru_{py})	LMCT π(pp) → dπ(Ru_{pp})	rLMCT π(py) → dπ(Ru_{pp})
1a^{4+}	32.9 (13.3)	25.2 (3.5)	20.6 (2.7)	8.5 (0.8)
	31.7 (12.9)	23.2 (3.1)	17.5 (1.9)	5.0 (0.2)
1b^{4+}	35.0 (27.5)	25.5 (4.6)	17.1 (1.9)	8.0 (1.7)
	32.0 (29.2)	23.2 (1.8)		
	29.6 (14.6)sh			
2a^{4+}	33.0 (16.3)	23.2 (4.8)		14.7 (1.8)sh
	31.8 (15.2)	20.3 (7.9)		7.1 (0.4)
		17.3(3.0)		
2b^{4+}	35.1 (26.0)	22.3 (4.		14.8 (1.3)sh
	32.8 (26.7)	20.1 (6.3)		
	32.0 (27.5)	17.4 (2.6)		
	29.5 (11.9)sh			

of these MLCT transitions, possibly with small contributions of dπ(Ru_{pp}) → dπ(Ru_{pp}) MC transitions.[32] For 1a−b^{3+}, no new band in the visible is clearly defined. Instead, a shift to higher energies is observed for the dπ(Ru_{pp}) → π^*(pp) MLCT bands (from 20900 cm^{-1} to a shoulder at 23200 cm^{-1} for 1a^{3+}). The dπ(Ru_{py}) → π^*(py) MLCT is also visible for 1a^{3+}, although less defined as a shoulder at 31600 cm^{-1} mounted on the π(bpy) → π^*(bpy) band at around 33500 cm^{-1}. Similar shifts have been observed in related binuclear complexes[17,33] and have their origin in the stabilization of the dπ(Ru_{pp}) orbitals by the presence of a Ru(III) ion coordinated to the cyanide bridge. This feature is not resolved in the case of 1b^{3+} because it is obscured by LC(tpy) bands that are red-shifted with respect to the LC(bpy) transition of 1a^{3+}.

The bottom parts of Figure 3 and Figure S2 in the Supporting Information illustrate spectral changes observed when the second electron is removed. The spectra of 2a−b^{4+} (Table 3) show a red shift of the π(MeOpy) → dπ(Ru_{py}) LMCT (~20000 cm^{-1}). This corresponds to a stabilization of Ru^{III}_{py} dπ acceptor orbitals by the presence of a Ru(III) neighbor, similar to the stabilization of the dπ(Ru_{pp}) orbitals previously discussed. Simultaneously, new low energy bands appear for 2a−b^{4+} around 15000 cm^{-1}, for which dπ(Ru_{pp}) are likely to be the acceptor orbitals. These bands are reminiscent of the transitions observed in the model compounds [Ru^{III}(T)(bpy)-(NCS)]$^{2+}$ (Figure S3 in the Supporting Information) and *cis*-[Ru(bpy)$_2$(NCS)$_2$]$^+$, and in the latter case, (TD)DFT assigns a π(S) → dπ(Ru_{pp}) character to it.[34] For 2a−b^{4+} (Table 3), our (TD)DFT calculations (see below and the Supporting Information) point to the π orbitals of the MeOpy as the donor orbital and hence are remote LMCT (rLMCT). Similarly, the spectrum of 1a−b^{4+} is dominated by LMCT transitions placed on both ruthenium centers.

SEC measurements in the near-infrared (NIR) for the one electron oxidation process reveal the presence of intense transitions associated with the mixed-valence species, that are absent for the completely reduced and the completely oxidized states (Table 2 and Figure 4 and Figure S4 in the Supporting Information). We assign them as IVCT bands. The band for 1a^{3+} clearly presents a structure with shoulders at higher and lower energies with respect to the maxima (maxima at 6300 cm^{-1} and shoulders at 8500 and 5100 cm^{-1}, Table 2). The band for 1b^{3+} is also asymmetric with a less defined shoulder on the high-energy side (maxima at 6000 cm^{-1} and shoulder at 8300 cm^{-1}). For 2a−b^{3+}, the IVCT bands appear in the same region, but show not structure. The bands observed for 1a−b^{3+}

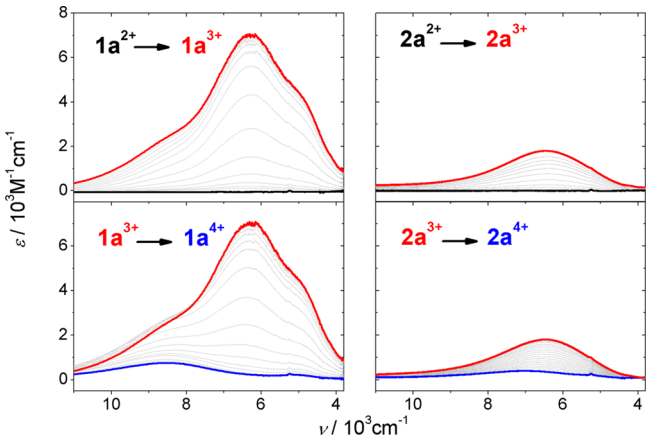

Figure 4. NIR spectroelectrochemistry of 1a (left) and 2a (right) in acetonitrile/0.1 M [TBA]PF_6, during the first (top) and second (bottom) oxidation processes. The spectra of the [II,II] (black), [III,II] (red), and [III,III] (blue) species are highlighted.

are very strong (ε at the maxima are 7100 and 7600 M^{-1} cm^{-1} for 1a^{3+} and 1b^{3+}, respectively), while the bands observed for 2a−b^{3+} are substantially less intense (ε = 1800 and 1000 M^{-1} cm^{-1} for 2a^{3+} and 2b^{3+}, respectively).

Oxidation of 1a−b^{3+} by a second electron (Figure 4 and Figure S4 in the Supporting Information) results in the loss of the strong IVCT bands and the appearance of a weaker band in this region (at 8500 and 8000 cm^{-1} for 1a^{4+} and 1b^{4+} respectively, Figure 4 and Figure S4 in the Supporting Information). These bands are absent in the model Ru(III) monomers, suggesting that they are LMCT transitions from the ligands in one Ru coordination sphere to a vacant orbital in the vicinal Ru(III) fragment. A weaker band is observed for 2a^{4+} in the same energy region (see Table 3), but not for 2b^{4+}, indicating that this complex may have a different electronic configuration.

IR Spectroscopy. We also explored the IR spectroscopy of all the redox states of complexes 1a−b and 2a−b. All the bimetallic complexes exhibit cyanide stretches between 2200 and 2000 cm^{-1}. Figure 5 and Figure S5 in the Supporting Information show the evolution of the IR spectra in acetonitrile for the complexes 1−2b^{2+} and 1−2a^{2+} respectively, during the first (top) and second (bottom) oxidation processes. The spectra of the reduced forms of all these molecules share the same characteristics in the region where the cyanide stretches are expected, showing an intense band at ~2070 cm^{-1} and a

dx.doi.org/10.1021/ic5002539 | Inorg. Chem. 2014, 53, 8221−8229

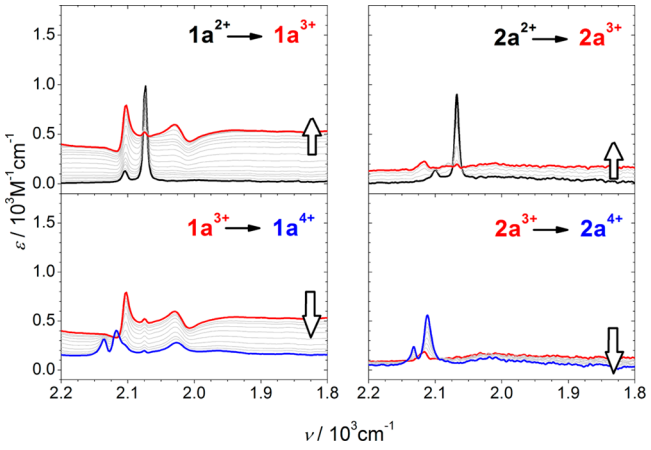

Figure 5. IR spectroelectrochemistry of **1a** (left) and **2a** (right) in acetonitrile/0.1 M [TBA]PF_6, during the first (top) and second (bottom) oxidation processes. The spectra of the [II,II] (black), [III,II] (red), and [III,III] (blue) species are highlighted. The white arrow illustrates the evolution of an electronic band.

weaker band around 2100 cm^{-1}. These bands correspond to the stretches of the two nonequivalent cyanide groups present in these molecules, the bridging cyanide and the terminal cyanide.

Upon their oxidation, a disparate behavior of the IR absorption profiles is observed for the complexes bearing different pyridines. **1a**–**b**$^{3+}$ present two cyanide stretches mounted on top of a wide band, probably of electronic character. The band at higher energies is more intense than the one observed for **1a**–**b**$^{2+}$, while the other is displaced to lower energies and becomes wider (Figure 5 and Figure S5 in the Supporting Information). For **2a**–**b**$^{3+}$ instead, the spectrum is surprisingly different; only two very weak cyanide stretches can be distinguished.

Further oxidation of the bimetallic complexes results in a new agreement between the IR spectra of all the complexes. The electronic band and the low energy cyanide stretch disappear in **1a**–**b**$^{4+}$, and they are replaced for two cyanide stretches above 2100 cm^{-1}. These last features are very similar to those observed for **2a**–**b**$^{4+}$. Assignments of the cyanide stretches are detailed in Table 4.

Table 4. IR Data in Acetonitrile/0.1 M [TBA]PF_6 for the Complexes 1a–b and 2a–b in Their Different Oxidation States

	ν_{CN} (ε)/cm^{-1} (M^{-1} cm^{-1})	
species	terminal	bridge
1a^{2+}	2104 (150)	2073 (1000)
1a^{3+}	2102 (800)	2029 (600)
1a^{4+}	2135 (300)	2117 (400)
1b^{2+}	2101 (200)	2073 (1650)
1b^{3+}	2103 (850)	2020 (650)
1b^{4+}	2134 (350)	2114 (500)
2a^{2+}	2100 (150)	2067 (900)
2a^{3+}	2123 (200)	2115 (250)
2a^{4+}	2132 (250)	2111 (600)
2b^{2+}	2097 (200)	2066 (1250)
2b^{3+}	2128 (200)	2117 (250)
2b^{4+}	2131 (300)	2108 (600)

DFT Results. Little success has been achieved in using DFT as a tool for analyzing the structure of some class II mixed-valence complexes.[35,36] This is due to the so-called "self-interaction error" that involves the residual interaction of an electron with itself.[37,38] This error results in an artificial stabilization of the delocalized state,[39,40] which leads to a wrong assignment of the configuration of the ground state for many complexes in class II of the Robin and Day classification.[41] Different approaches have been proposed to overcome this limitation in some specific systems,[42,43] although this problem remains a challenge for this technique.[44] On the other hand, standard DFT calculations can predict very accurately the properties of class III, delocalized systems,[35,5] and we have proposed that the match between the predicted and the observed spectra of a mixed-valence complex can be used to assign the delocalized nature of its ground state.[5]

We have used regular DFT to explore the structure and spectroscopy of all the redox states of the four bimetallic complexes reported here. The calculated structure of the **1b**$^{2+}$ binuclear complex reproduces the experimentally observed one,[18] an almost perfect linear arrangement of the atoms involved in the cyanide bridge, the propeller-like configuration for the *trans*-{Ru(py)$_4$} fragment, and a distorted octahedral configuration for the {Ru(tpy)(bpy)} unit. These characteristics are retained in the computed structure of the four bimetallic complexes in their different redox states (Table S1 in the Supporting Information) with no significant differences noted as it has been observed experimentally for other cyanide-bridged systems.[45] The exceptions are the Ru–N_{MeOpy} distances for the binuclear complexes **2a**–**b**, which are sensitive to the redox state of the ruthenium. For example, the oxidation of the *trans*-{Ru(MeOpy)$_4$} moiety in the [III,II] mixed-valence state is accompanied by a reduction of the Ru–N distance as expected for an oxidation of the ruthenium center.[4] For the bimetallic complexes **1a**–**b** instead, the computed structures of the [III,II] mixed-valence state show no difference in the Ru–N distances for both metallic ions.

In agreement with the previous result, the calculated spin densities suggest that the bimetallic complexes **1a**–**b**$^{3+}$ have a different configuration than the one predicted for **2a**–**b**$^{3+}$. The computed spin density of **1a**–**b**$^{3+}$ is delocalized over the Ru–CN–Ru fragment, while it is completely localized on the Ru_{py} for **2a**–**b**$^{3+}$. For the latter complexes the spin density is confined to the plane perpendicular to the cyanide bridge, suggesting that the hole in the Ru^{III}_{py} corresponds to the d_{xy} orbital (Figure 6 and Figure S6 in the Supporting Information).

The spectroscopy of the **1a**–**b**$^{3+}$ complexes provided by the (TD)DFT agrees well with the detected properties of these mixed-valence complexes (Figure 7 and Figure S7 in the Supporting Information). These results indicate that the ground state description supplied by the DFT is in agreement with the experimental behavior. For the mixed-valence complex **1a**$^{3+}$, the DFT calculation predicts an intense transition in the NIR at nearly the same energy (6475 cm^{-1}) where it is experimentally observed (6300 cm^{-1}, Figure 7). This transition corresponds almost exclusively to a transition between the HOMO and the LUMO of the molecule, both of which comprise the two ruthenium fragments and the cyanide bridge (Figure S10 in the Supporting Information). The (TD)DFT also predicts less intense IVCT bands at 8850 and 5500 cm^{-1} that are very close to the observed shoulders in the experimental band. Also weaker bands are predicted in the

dx.doi.org/10.1021/ic5002539 | Inorg. Chem. 2014, 53, 8221–8229

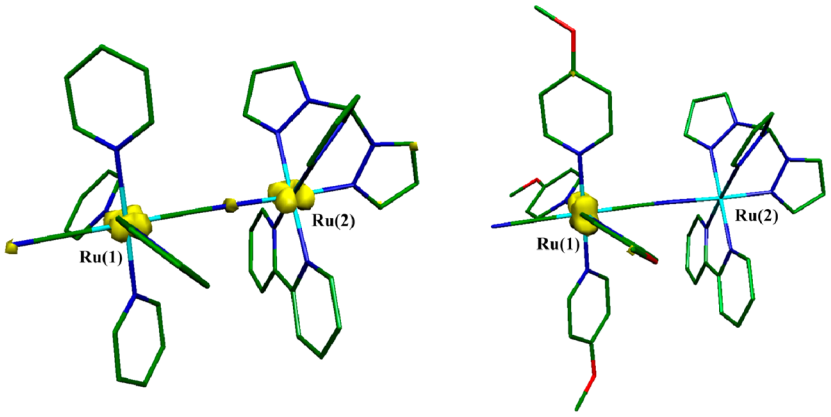

Figure 6. Computed spin density (0.02 au) for the doublet $\mathbf{1a}^{3+}$ (left) and $\mathbf{2a}^{3+}$ (right) ions.

Table 5. Mulliken Spin Densities for the Doublet $\mathbf{1a–b}^{3+}$ and $\mathbf{2a–b}^{3+}$ Ions

	Mulliken spin densities	
species	Ru(1)	Ru(2)
$\mathbf{1a}^{3+}$	0.447	0.493
$\mathbf{2a}^{3+}$	0.941	0.000
$\mathbf{1b}^{3+}$	0.408	0.545
$\mathbf{2b}^{3+}$	0.939	0.000

visible, mainly of MLCT character (Figure 7 and Table S2 in the Supporting Information).

The (TD)DFT results for $\mathbf{2a–b}^{3+}$ reproduce well the pattern observed in their electronic spectra (Figure 7 and Figure S7 in the Supporting Information), including the presence of two LMCT from the MeOpy ligand to the Ru^{III}_{py} ion, and two MLCT transitions from the Ru^{II}_{pp} to the bpy at higher energies. The predicted spectrum for $\mathbf{2a}^{3+}$ also presents a weak band around 7000 cm^{-1} (Figure 7), which corresponds mainly to IVCT transitions from a Ru_{pp} $d\pi$ orbital to a vacant Ru_{py} d_{xy} orbital. Due to the different orientation of the orbitals, the transition is predicted to be weak as observed experimentally.

The behavior of the calculated IR spectra of these binuclear complexes also agrees with the observed, including the displacement to lower energies of the cyanide-bridge stretching frequency observed for $\mathbf{1a–b}^{3+}$, but not for $\mathbf{2a–b}^{3+}$ (Figure 7 and Figure S7 in the Supporting Information). In the same IR region, (TD)DFT predicts electronic transitions at around 2500 and 2000 cm^{-1} for $\mathbf{1a–b}^{3+}$ and $\mathbf{2a–b}^{3+}$ respectively. These are intraconfigurational (IC) transitions between $d\pi$ orbitals split by the departure from the octahedral geometry of the coordination sphere of the Ru_{py}. The positions of these bands match well with the wide band that raises the vibrational spectra of $\mathbf{1a–b}^{3+}$ (Figure 7) and $\mathbf{2a–b}^{3+}$ (Figure S10 in the Supporting Information). This agreement is surprisingly satisfactory, as the DFT calculation does not include the

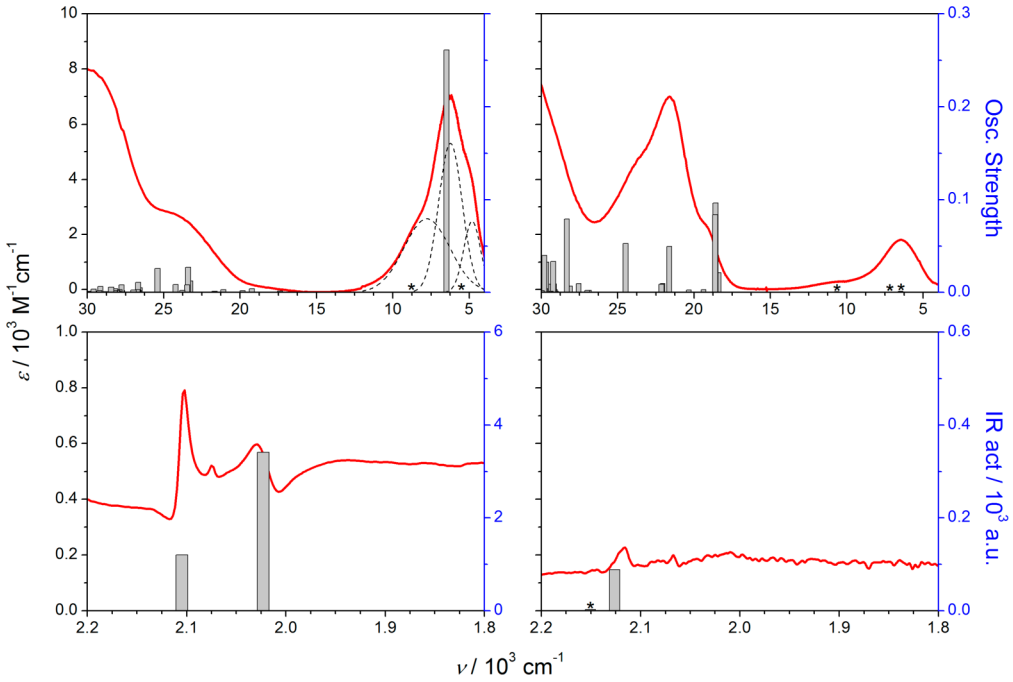

Figure 7. Comparison of the NIR (top) and IR (bottom) spectra of $\mathbf{1a}^{3+}$ (left) and $\mathbf{2a}^{3+}$ (right) in acetonitrile/0.1 M $[TBA]PF_6$ and the energy of the transitions/vibrations predicted by the DFT calculations (bars). The * denotes the energy of predicted transitions with an oscillator strength near or equal to zero.

dx.doi.org/10.1021/ic5002539 | *Inorg. Chem.* 2014, 53, 8221–8229

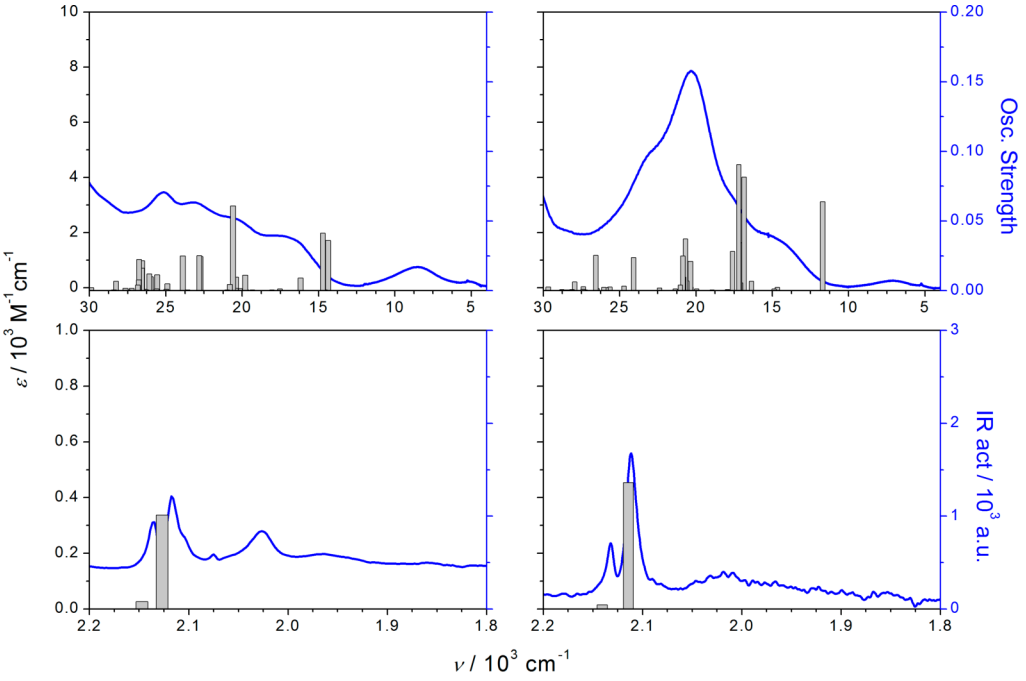

Figure 8. Comparison of the NIR (top) and IR (bottom) spectra of $\mathbf{1a}^{4+}$ (left) and $\mathbf{2a}^{4+}$ (right) in acetonitrile/0.1 M $[TBA]PF_6$ and the energy of the transitions/vibrations predicted by the DFT calculations (bars). The * denotes the energy of predicted transitions with an oscillator strength near or equal to zero.

spin−orbit interaction that may also play a role in the energy of these transitions.

The (TD)DFT calculation also gives a qualitative interpretation of the rich spectroscopy of the [III,III] redox state of these complexes, but fails to predict the correct energy, usually providing a lower value than that observed experimentally (Table S27 in the Supporting Information). The more intense transition calculated for $\mathbf{2a-b}^{4+}$ (Figure 8 and Figure S8 and Tables S23 and S25 in the Supporting Information) is from the MeOpy ligand to the vicinal Ru^{III}_{py} At lower energies, the (TD)DFT calculations predict rLMCT transitions from the MeOpy ligand, this time to the distant Ru^{III}_{pp} center that we assign as the transitions observed around 15000 cm^{-1} in the experimental spectra. For $\mathbf{1a-b}^{4+}$, the computed spectra (Figure 8 and Figure S8 in the Supporting Information) involve a series of low intensity LMCT bands centered in both ruthenium ions (Table 3). At lower energies, the (TD)DFT calculation for $\mathbf{1a}^{4+}$ also predicts a remote LMCT from the pyridine ligands to the distant Ru^{III}_{py}, which we assign as the transition observed at 8500 cm^{-1}. For $\mathbf{1b}^{4+}$ a similar transition is observed experimentally, but it is not predicted by the (TD)DFT; instead an IC band is predicted in the same region. The different nature of the band predicted has its origin in diverse configuration of the calculated ground state for $\mathbf{1a}^{4+}$ and $\mathbf{1b}^{4+}$ (Figures S27 and S28 in the Supporting Information). In contrast, the similitudes in the experimental spectra of these species suggest that both complexes have the same configuration and that the DFT is predicting the wrong one for $\mathbf{1b}^{4+}$. The spectrum of $\mathbf{2a}^{4+}$ also presents the rLMCT transition in the NIR region, although with a smaller intensity, while it is absent for both the calculated and the observed spectra of $\mathbf{2b}^{4+}$. Moreover, the (TD)DFT predicts electronic transitions in the IR of a similar IC origin as the one reported for $\mathbf{1a-b}^{3+}$. These bands are detectable in the experimental spectra (Figure S11 and Table S4 in the Supporting Information).

DISCUSSION

We prepared the complexes **1a−b** to explore their mixed-valence properties. Our hypothesis was that, in the d^6-d^5 system, a small difference between the energies of the $d\pi$ orbitals of the two ions linked by a cyanide bridge should result in a delocalized system, i.e., a system where an unpaired electron is equally distributed between the two metallic centers. This requires compensating for the differential effect of the cyanide ion on the energies of the $d\pi$ orbitals of the ruthenium ions bridged. Following this idea, we have observed evidence of delocalization in two trimetallic complexes, *trans*-$[(dmap)_4Ru\{(\mu\text{-}NC)OsCN_5\}_2]^{4-}$ [4] and *trans*-$[(dmap)_4Ru\{(\mu\text{-}CN)Ru(py)_4Cl\}_2]^{3+}$.[5] In the first case the compensation of the effect of the cyanide was achieved thanks to the different metallic ions involved and the specific solvent effect on the terminal cyanides,[46] while in the second the energies of $d\pi$ orbitals were balanced through the use of different substituents on the pyridine rings of the ruthenium ions. The $\mathbf{1a-b}^{3+}$ complexes are simple bimetallic systems, representative of the hundreds of mixed-valence cyanide compounds reported in the literature. In this case, we expect that the energies of the $d\pi$ orbitals of the Ru ions should be similar due to the incorporation of the polypyridine ligands on the Ru ion bound to the N end of the cyanide bridge, which are better acceptor ligands than the pyridines coordinated to the C bound Ru ion.

The NIR bands observed for $\mathbf{1a-b}^{3+}$ are remarkable. As expected from the smaller ΔE between the ruthenium couples, they are more intense and shifted to the red compared to similar bimetallic systems.[17,33,47] However, unlike the previously studied systems, the signal is actually the overlap of three IVCT bands, particularly well resolved for $\mathbf{1a}^{3+}$ in acetonitrile, but discernible in all the solvents explored (Figure 4 and Figure S9 in the Supporting Information). A deconvolution in Gaussian bands of the observed NIR absorbance reveals that the transitions at lower energies, at

dx.doi.org/10.1021/ic5002539 | Inorg. Chem. 2014, 53, 8221−8229

4800 and 6200 cm^{-1}, have narrow bandwidths (1300 and 1900 cm^{-1}, Figure 7 and Figure S9 and Table S2 in the Supporting Information), while the band at higher energies, at 8000 cm^{-1}, is considerably wider (3000 cm^{-1}). The narrowness of these transitions facilitates the resolution of the three components of the band. For $\mathbf{1b}^{3+}$ a similar deconvolution is also possible, but the resulting transitions are slightly wider, making more difficult their detection, although they are more apparent in methanol (Figure S9 in the Supporting Information). The energy and width of these bands are mainly solvent independent, even though their intensity shows some dependence (Figure S9 in the Supporting Information). The very weak influence of the solvent on the energy of these transitions is notable considering that these complexes have one terminal cyanide ligand and some specific interaction with the solvent is expected.[48]

The observation of three IVCT bands has been previously reported for the ruthenium dimer $[Cl_3Ru(tppz)RuCl_3]^-$ (tppz = 2,3,5,6-tetrakis(2-pyridyl)pyrazine).[13] This compound has been classified as a class II–III system,[13] due to the solvent independent nature of the observed narrow IVCT bands, which indicates valence averaging on the time scale of the solvent motions.[11,12,49] The same argument applies for the two lower energy IVCT bands observed for $\mathbf{1a–b}^{3+}$, where the solvent seems not to participate in the reorganizational energy (λ) associated with these transitions. The IVCT band at higher energies instead behaves like a regular IVCT. The persistence of the two MLCT bands in the mixed-valence species, shifted to higher energies, is likewise compatible with the partial oxidation of both ruthenium ions, as opposed to the oxidation of one single center that should result in the loss of one MLCT band as observed for $\mathbf{2a–b}^{3+}$.

The IR spectra of the $\mathbf{1a–b}^{3+}$ is compatible with this description as well. The main feature is the shift of a cyanide stretch to lower energies that is accompanied by an increase in intensity and bandwidth. The latter behavior is probably due to the vibronic coupling of the stretching of cyanide bridge with the IVCT as proposed for other cyanide-[33,50] and pyrazine-bridged[51] mixed-valence systems. It is interesting to note that the intensification observed for this stretch in $\mathbf{1a–b}^{3+}$ is less pronounced than that observed in some related complexes.[17,33,52] This trend is compatible with a more uniform charge distribution in these molecules, which results in a smaller change in the dipolar moment associated with this stretch.

The (TD)DFT calculations performed on $\mathbf{1a–b}^{3+}$ reproduce well their spectroscopy and confirm the delocalized description. The computed spin density of $\mathbf{1b}^{3+}$ shows similar spin densities for both ruthenium centers (Ru_{py} = 0.41 and Ru_{pp} = 0.55), while the distribution computed for $\mathbf{1a}^{3+}$ is even more uniform (Ru_{py} = 0.44 and Ru_{pp} = 0.49). So the electron density in these complexes extends over the two ruthenium ions, although the distribution is not equal, given the different nature of both centers. The lack of symmetry of these systems put them in class II–III, although there is no evidence of the presence of the two electronic isomers associated with two minima in their potential energy surfaces.

We explored the spectroscopy of $\mathbf{2a–b}^{3+}$, looking to characterize a more localized version of these bimetallic complexes. Instead, we found that their properties are surprisingly different, for example the intensity of the IVCT band is significantly lower than the one observed in related systems.[17,33,47] The DFT results point to a different electronic configuration as the origin of this different behavior. In these complexes, the LUMO is located at a d_{xy} orbital centered at the Ru_{py} moiety and perpendicular to the cyanide bridge. The higher energy of d_{xy} orbital is due to more basic character of the MeOpy ligand. This orientation precludes an extensive coupling with the Ru_{pp} centered $d\pi$ orbitals and results in a localization of the charge and less intense and wider IVCT transitions whose energy maximum depends on the nature of the solvent (Figure S10 in the Supporting Information). Another significant difference observed is the modest intensity of the cyanide-bridge stretches. Presumably, the different orientation of the LUMO in $\mathbf{2a–b}^{3+}$ prevents their vibronic coupling with the IVCT. This result underlines the importance of this mechanism in the high intensity of the cyanide stretch, frequently observed in many mixed-valence complexes.[17,33,50,52–57]

CONCLUSIONS

The complexes $\mathbf{1a–b}^{3+}$ exhibit two IVCT bands with very narrow bandwidth that allowed their resolution in the spectra. This property and the weak solvent dependence of the energy of these transitions suggest that these systems belong to class II–III, proposed by Meyer and co-workers,[11] that extends the Robin and Day classification. DFT calculation confirms an extensive delocalization through the ruthenium centers and the cyanide bridge, although the electron density is not evenly distributed. In these systems, delocalization is achieved through the different coordination spheres of the rutheniums linked by the cyanide bridge.

Localization of the hole in the d_{xy} orbital of the Ru_{py} results in a much weaker coupling between the ruthenium centers. The big impact of the electronic configuration in the properties of a mixed-valence complex is well illustrated by the contrasting spectroscopies of $\mathbf{2a–b}^{3+}$ and $\mathbf{1a–b}^{3+}$.

ASSOCIATED CONTENT

Supporting Information

^{1}H NMR, vis–NIR, UV–vis, NIR, and IR spectra and additional experimental and computational details. This material is available free of charge via the Internet at http://pubs.acs.org.

AUTHOR INFORMATION

Corresponding Author

*E-mail: baraldo@qi.fcen.uba.ar.

Notes

The authors declare no competing financial interest.

ACKNOWLEDGMENTS

The authors thank the University of Buenos Aires and the Consejo Nacional de Investigaciones Científicas y Técnicas (CONICET) for funding. G.E.P. thanks Adrián Roitberg for selflessly sharing his knowledge. B.M.A.-T. and A.C. thank periodic technical assistance by Argentinean Logistic Network (ALN). L.B.V. is a member of the scientific staff of CONICET; A.C. is a postdoctoral fellow of the same institution. B.M.A.-T. is a graduate fellow of UBA.

REFERENCES

(1) Creutz, C.; Taube, H. *J. Am. Chem. Soc.* **1969**, *91*, 3988–3989.
(2) Endicott, J. F.; Chen, Y.-J. *Coord. Chem. Rev.* **2013**, *257*, 1676–1698.

(3) Shatruk, M.; Avendaño, C.; Dunbar, K. R. In *Progress in Inorganic Chemistry*; John Wiley & Sons, Inc.: Hoboken, NJ, 2009; Vol. *56*, pp 155−334.
(4) Rossi, M. B.; Abboud, K. A.; Alborés, P.; Baraldo, L. M. *Eur. J. Inorg. Chem.* **2010**, 5613−5616.
(5) Pieslinger, G. E.; Alborés, P.; Slep, L. D.; Baraldo, L. M. *Angew. Chem., Int. Ed.* **2014**, *53*, 1293−1296.
(6) Hush, N. S. *Prog. Inorg. Chem.* **1967**, *8*, 391−444.
(7) Hush, N. S. *Electrochim. Acta* **1968**, *13*, 1005−1023.
(8) Sutin, N. *Prog. Inorg. Chem.* **1983**, *30*, 441−498.
(9) Marcus, R. A.; Sutin, N. *Biochim. Biophys. Acta* **1985**, *811*, 265−322.
(10) Neyhart, G. A.; Timpson, C. J.; Bates, W. D.; Meyer, T. J. *J. Am. Chem. Soc.* **1996**, *118*, 3730−3737.
(11) Demadis, K. D.; Hartshorn, C. M.; Meyer, T. J. *Chem. Rev.* **2001**, *101*, 2655−2685.
(12) Concepcion, J. J.; Dattelbaum, D. M.; Meyer, T. J.; Rocha, R. C. *Philos. Trans. Ser. A* **2008**, *366*, 163−175.
(13) Rocha, R. C.; Rein, F. N.; Jude, H.; Shreve, A. P.; Concepcion, J. J.; Meyer, T. J. *Angew. Chem., Int. Ed.* **2008**, *47*, 503−506.
(14) Llobet, A.; Doppelt, P.; Meyer, T. J. *Inorg. Chem.* **1988**, *27*, 514−520.
(15) Takeuchi, K. J.; Thompson, M. S.; Pipes, D. W.; Meyer, T. J. *Inorg. Chem.* **1984**, *23*, 1845−1851.
(16) Coe, B. J.; Meyer, T. J.; White, P. S.; Meyer, J. T. J. *Inorg. Chem.* **1995**, *34*, 593−602.
(17) Pieslinger, G. E.; Alborés, P.; Slep, L. D.; Coe, B. J.; Timpson, C. J.; Baraldo, L. M. *Inorg. Chem.* **2013**, *52*, 2906−2917.
(18) Cadranel, A.; Aramburu Trošelj, B. M.; Yamazaki, S.; Alborés, P.; Kleiman, V. D.; Baraldo, L. M. *Dalton Trans.* **2013**, *42*, 16723−16732.
(19) Noviandri, I.; Brown, K. N.; Fleming, D. S.; Gulyas, P. T.; Lay, P. A.; Masters, A. F.; Phillips, L. *J. Phys. Chem. B* **1999**, *103*, 6713−6722.
(20) Kaim, W.; Fiedler, J. *Chem. Soc. Rev.* **2009**, *38*, 3373−3382.
(21) Frisch, M. J.; Trucks, G. W.; Schlegel, H. B.; Scuseria, G. E.; Robb, M. A.; Cheeseman, J. R.; Scalmani, G.; Barone, V.; Mennucci, B.; Petersson, G. A.; Nakatsuji, H.; Caricato, M.; Li, X.; Hratchian, H. P.; Izmaylov, A. F.; Bloino, J.; Zheng, G.; Sonnenberg, J. L.; Hada, M.; Ehara, M.; Toyota, K.; Fukuda, R.; Hasegawa, J.; Ishida, M.; Nakajima, T.; Honda, Y.; Kitao, O.; Nakai, H.; Vreven, T.; Jr; Peralta, J. E.; Ogliaro, F.; Bearpark, M.; Heyd, J. J.; Brothers, E.; Kudin, K. N.; Staroverov, V. N.; Kobayashi, R.; Normand, J.; Raghavachari, K.; Rendell, A.; Burant, J. C.; Iyengar, S. S.; Tomasi, J.; Cossi, M.; Rega, N.; Millam, J. M.; Klene, M.; Knox, J. E.; Cross, J. B.; Bakken, V.; Adamo, C.; Jaramillo, J.; Gomperts, R.; Stratmann, R. E.; Yazyev, O.; Austin, A. J.; Cammi, R.; Pomelli, C.; Ochterski, J. W.; Martin, R. L.; Morokuma, K.; Zakrzewski, V. G.; Voth, G. A.; Salvador, P.; Dannenberg, J. J.; Dapprich, S.; Daniels, A. D.; Farkas; Foresman, J. B.; Ortiz, J. V; Cioslowski, J.; Fox, D. J. *Gaussian 09 Rev. C.01*; Gaussian, Inc.: Wallingford, CT, 2009.
(22) Szabo, A.; Ostlund, N. S. *Modern Quantum Chemistry: Introduction to Advanced Electronic Structure Theory*; McGraw-Hill: New York, 1989.
(23) Scalmani, G.; Frisch, M. J. *J. Chem. Phys.* **2010**, *132*, 114110.
(24) Tomasi, J.; Mennucci, B.; Cammi, R. *Chem. Rev.* **2005**, *105*, 2999−3093.
(25) Miertuš, S.; Scrocco, E.; Tomasi, J. *Chem. Phys.* **1981**, *55*, 117−129.
(26) Schlegel, H. B. *J. Comput. Chem.* **1982**, *3*, 214−218.
(27) Petit, L.; Maldivi, P.; Adamo, C. *J. Chem. Theory Comput.* **2005**, *1*, 953−962.
(28) Stratmann, R.; Scuseria, G.; Frisch, M. J. *J. Chem. Phys.* **1998**, *109*, 8218−8224.
(29) Flükiger, P.; Lüthi, H. P.; Portmann, S.; Weber, J. *MOLEKEL 4.3*.
(30) Portmann, S.; Luthi, H. *Chimia* **2000**, *54*, 766−770.
(31) O'Boyle, N. M.; Tenderholt, A. L.; Langner, K. M. *J. Comput. Chem.* **2008**, *29*, 839−845.
(32) Crosby, G. A. *Acc. Chem. Res.* **1975**, *8*, 231.
(33) Macatangay, A. V.; Endicott, J. F. *Inorg. Chem.* **2000**, *39*, 437−446.
(34) Kaemper, S.; Paretzki, A.; Fiedler, J.; Zalis, S.; Kaim, W. *Inorg. Chem.* **2012**, *51*, 2097−2104.
(35) Braun-Sand, S. B.; Wiest, O. *J. Phys. Chem. A* **2003**, *107*, 285−291.
(36) Lundberg, M.; Siegbahn, P. E. M. *J. Chem. Phys.* **2005**, *122*, 224103.
(37) Zhang, Y.; Yang, W. *J. Chem. Phys.* **1998**, *109*, 2604−2608.
(38) Perdew, J. P.; Levy, M. *Phys. Rev. B* **1997**, *56*, 16021−16028.
(39) Cohen, A. J.; Mori-Sánchez, P.; Yang, W. *Science* **2008**, *321*, 792−794.
(40) Vydrov, O. A.; Scuseria, G. E.; Perdew, J. P. *J. Chem. Phys.* **2007**, *126*, 154109.
(41) Robin, M. B.; Day, P. *Adv. Inorg. Chem. Radiochem.* **1968**, *10*, 247.
(42) Kaduk, B.; Kowalczyk, T.; Van Voorhis, T. *Chem. Rev.* **2012**, *112*, 321−370.
(43) Cai, Z.-L.; Crossley, M. J.; Reimers, J. R.; Kobayashi, R.; Amos, R. D. *J. Phys. Chem. B* **2006**, *110*, 15624−15632.
(44) Cohen, A. J.; Mori-Sánchez, P.; Yang, W. *Chem. Rev.* **2012**, *112*, 289−320.
(45) Ma, X.; Hu, S.-M.; Tan, C.-H.; Wen, Y.-H.; Zhu, Q.-L.; Shen, C.-J.; Sheng, T.-L.; Wu, X.-T. *Dalton Trans.* **2012**, *41*, 12163−12169.
(46) Rossi, M. B.; Alborés, P.; Baraldo, L. M. *Inorg. Chim. Acta* **2011**, *374*, 334−340.
(47) Watzky, M. A.; Macatangay, A. V.; VanCamp, R. A.; Mazzetto, S. E.; Song, X. Q.; Endicott, J. F.; Buranda, T. *J. Phys. Chem. A* **1997**, *101*, 8441−8459.
(48) Timpson, C. J.; Bignozzi, C. A.; Sullivan, B. P.; Kober, E. M.; Meyer, T. J. *J. Phys. Chem.* **1996**, *100*, 2915−2925.
(49) D'Alessandro, D. M.; Keene, F. R. *Chem. Soc. Rev.* **2006**, *35*, 424−440.
(50) Watzky, M. a.; Endicott, J. F.; Song, X.; Lei, Y.; Macatangay, A. V. *Inorg. Chem.* **1996**, *35*, 3463−3473.
(51) Rocha, R. C.; Shreve, A. P. *Chem. Phys.* **2006**, *326*, 24−32.
(52) Roncaroli, F.; Baraldo, L. M.; Slep, L. D.; Olabe, J. A. *Inorg. Chem.* **2002**, *41*, 1930−1939.
(53) Siddiqui, S.; Henderson, W. W.; Shepherd, R. E. *Inorg. Chem.* **1987**, *26*, 3101−3107.
(54) Cutin, E. H.; Katz, N. E. *Polyhedron* **1993**, *12*, 955−960.
(55) Laidlaw, W. M.; Denning, R. G. *J. Chem. Soc., Dalton Trans.* **1994**, 1987−1994.
(56) Pfennig, B. W.; Fritchman, V. A.; Hayman, K. A. *Inorg. Chem.* **2001**, *40*, 255−263.
(57) Sheng, T.-L.; Vahrenkamp, H. *Eur. J. Inorg. Chem.* **2004**, 1198−1203.